

Elucidating the Effect of Planar Graphitic Layers and Cylindrical Pores on the Storage and Diffusion of Li, Na, and K in Carbon Materials

Emilia Olsson, Jonathon Cottom, Heather Au, Zhenyu Guo, Anders C. S. Jensen, Hande Alptekin, Alan J. Drew, Maria-Magdalena Titirici, and Qiong Cai*

Hard carbons are among the most promising materials for alkali-ion metal anodes. These materials have a highly complex structure and understanding the metal storage and migration within these structures is of utmost importance for the development of next-generation battery technologies. The effect of different carbon structural motifs on Li, Na, and K storage and diffusion are probed using density functional theory based on experimental characterizations of hard carbon samples. Two carbon structural models—the planar graphitic layer model and the cylindrical pore model—are constructed guided by small-angle X-ray scattering and transmission electron microscopy characterization. The planar graphitic layers with interlayer distance <6.5 Å are beneficial for metal storage, but do not have significant contribution to rapid metal diffusion. Fast diffusion is shown to take place in planar graphitic layers with interlayer distance >6.5 Å, when the graphitic layer separation becomes so wide that there is negligible interaction between the two graphitic layers. The cylindrical pore model, reflecting the curved morphology, does not increase metal storage, but significantly lowers the metal migration barriers. Hence, the curved carbon morphologies are shown to have great importance for battery cycling. These findings provide an atomic-scale picture of the metal storage and diffusion in these materials.

1. Introduction

Next-generation battery technologies for electrochemical energy storage are receiving increasing attention due to the need to transition from a fossil fuel-based economy to a sustainable and renewable energy economy. These battery technologies have high efficiency, and are possible to further integrate with other renewable energy sources such as solar, hydro, and wind power. Lithium ion batteries (LIBs), which are currently utilized for energy storage in electric vehicles and portable devices, have high energy density and good cycle life, but are unsuitable for widespread use as grid scale energy storage, due to the Earth's limited and geographically localized lithium resources. Hence, alternative batteries based on other alkali metals such as sodium (Na) and potassium (K) have been researched due to their high abundance and low cost.^[1] K, like Li, forms

intercalation compounds with the common LIB anode material graphite, with similar theoretical concentration limit as that of Li (KC_8 vs LiC_6).^[2–4] The lattice parameters of KC_8 do however show that K intercalation compounds cause a wider interlayer spacing ($5.2^{[2]}$ and 5.35 Å^[5]) and expand the graphite lattice.^[4,5] A recent study concluded that Li intercalation into graphite is always energetically favorable from the calculation of formation energies, but that the formation of stable K-intercalation compounds is highly dependent on structural deformation of the graphite lattice.^[4] However, it has been shown that the common LIB anode material graphite is not suitable for Na-ion battery (NIB) applications, as Na only forms NaC_{64} .^[1,3] Hence, efforts seeking to develop low cost, high capacity, and durable NIB anode materials have been made. One such anode material is hard carbon, which has also been shown to be suitable as LIB and potassium ion battery (KIB) anodes.^[6–9] The exact nature of the metal storage and migration mechanisms in hard carbon materials remains one of the most urgent topics to be understood to realize the potential of NIBs and KIBs, and to offer an alternative to graphite in LIBs.^[10–13]


Hard carbon can be successfully produced from a wide range of biomass, making it especially interesting from a

Dr. E. Olsson, Dr. Q. Cai
Department of Chemical and Process Engineering
University of Surrey
Guildford GU2 7XH, UK
E-mail: q.cai@surrey.ac.uk

Dr. J. Cottom
Department of Physics and Astronomy
University College London
London WC1E 6BT, UK

Dr. H. Au, Z. Guo, H. Alptekin, Prof. M.-M. Titirici
Department of Chemical Engineering
Imperial College London
South Kensington Campus, London SW7 2AZ, UK

Dr. A. C. S. Jensen, Prof. A. J. Drew
School of Physics and Astronomy
Queen Mary University London
London E1 4NS, UK

 The ORCID identification number(s) for the author(s) of this article can be found under <https://doi.org/10.1002/adfm.201908209>.

© 2020 The Authors. Published by WILEY-VCH Verlag GmbH & Co. KGaA, Weinheim. This is an open access article under the terms of the Creative Commons Attribution License, which permits use, distribution and reproduction in any medium, provided the original work is properly cited.

DOI: 10.1002/adfm.201908209

sustainability viewpoint and a circular economy.^[12,14–20] The structure of hard carbon is highly complex and consists of randomly oriented graphitic layers.^[21,22] These graphitic layers, in turn, form different carbon motifs, leading to the presence of few-layer thick graphitic stacks, curved graphitic sheets, wide interlayer distance planar graphitic pores, and nanopores.^[23–26] The nanopores and wide planar graphitic layer pores have been suggested to aid metal diffusion, but the exact effect of hard carbon microstructure on both metal storage and diffusion remains unsolved.^[26] Typically, two distinct voltage regions are observed in the discharge profiles when studying Na storage in hard carbon materials: the sloping region (0.1 V and above), and a plateau region (0.1 V and below).^[27] The exact mechanism of Na storage in these two regions is still being debated. However, what is clear is that the Na storage mechanisms are dependent on the local structure and that there are a few main carbon motifs possibly responsible for the different metal storage and diffusion mechanisms.^[23,25,28,29] The dependence of local structure on the Na diffusion coefficients was also recently probed by Alvin et al.,^[30] showing that the Na diffusion coefficients and behavior in the different voltage regions has contributions from Na adsorption on surfaces and defects, on micropores, and from intercalation between graphitic sheets.^[30] These different storage mechanisms in the different carbon motifs that form the complex hard carbon structure will be discussed in the next section.

First, Na storage has been suggested to take place on defect sites in graphitic sheets, and both Li and K adsorption in hard carbon are assisted by these defects.^[20,27,31–34] Li, Na, and K storage on defective graphene was the topic of our previous publication, which confirmed that metal storage can be improved at defect sites, with certain defect sites acting as metal trapping sites due to high metal migration barriers.^[35] The metal storage on defect sites will hence not be further studied in this paper, and will only be referred to for comparing the metal storage and diffusion rates between different carbon motifs. Second, intercalation of metal ions in planar graphitic stacks contributes to metal storage capacity. Third, metal adsorption in micropores with different pore shapes has been suggested to contribute to the hard carbon metal storage and diffusion. These pores have a wide range of pore diameters (which could also be referred to as interlayer distances for the planar graphitic layer micropores), ranging up to around 5 nm.^[29,30,36,37] Experimental studies have shown that the interlayer distance of the planar graphitic layers in hard carbons has a direct influence on the ability to insert and extract Na, with interlayer distances of up to 8 Å reported.^[29,30] It has also been shown that, apart from the planar graphitic layers, curved and rumpled domains are present in hard carbon systems.^[9,38–44] To fully understand the effect of carbon structure on metal storage mechanisms, it is important to have an atomic scale study to bring insight into how the different isolated local carbon structures influence metal adsorption, binding, and migration, to further develop and commercialize these battery technologies.

This study aims to provide an atomistic view of the alkali metal storage in the range of pore sizes and shapes identified from structural characterization of hard carbon samples by investigating alkali metal adsorption and diffusion in two

carbon pore models—the planar graphitic layer and the cylindrical pore. We also study the metal intercalation in the graphitic stacks with interlayer distances between 3.3 and 4 Å (which based on our experimental characterization, is the range of interlayer distances in the graphitic stacks), to assess at what point these interlayer regions become accessible for Li, Na, and K storage. To consider the effect of cylindrical pores, we employ single wall carbon nanotube (CNT) models with different pore diameters. The cylindrical pore models would further be transferrable to provide atomistic insights into CNT anodes, which have previously been investigated for LIBs,^[45–51] NIBs,^[45–47,52–54] and KIBs.^[55] Finally, a mixed morphology model, combining both planar and curved regions are investigated for changes in metal binding energy going from a planar to a curved regime. The choices of the graphitic layer distance and the diameter of the cylindrical pore were guided by the experimentally measured characteristics of the hard carbon samples derived from glucose. This study provides fundamental insights into how different local structures contribute to the battery performance, in terms of favorable storage and diffusion sites. These insights could help the development of more efficient and engineered hard carbon anodes.

2. Results and Discussion

2.1. Experimental Characterization

Figure 1 shows the structural characterization of hard carbon samples prepared from hydrothermally treated glucose at different pyrolysis temperatures. With increasing carbonization temperature, wide-angle X-ray scattering (WAXS) showed a decreasing range of interlayer distances from 3.9 Å at 1000 °C to 3.33 Å at 1900 °C (Figure 1f), which is comparable to the interlayer distance of graphite. Similarly, a range of pore sizes were seen in the sample, with the pore size increasing with the increasing temperature, from ≈1.2 nm at 1000 °C to 5.1 nm at 1900 °C (Figure 1c). In contrast, however, N₂ adsorption measurements indicate that the accessible surface area and pore volume decrease dramatically for samples prepared above 1000 °C (Table S3, Supporting Information), suggesting the presence of closed porosity at higher temperatures. This trend is observable in the galvanostatic profiles and cyclic voltammograms (Figures S4–S6, Supporting Information) when tested against Li, Na and K, where G1000 shows the most pronounced irreversible behavior, for all metals, due to the greater surface available for solid electrolyte interface (SEI) formation.

To assess the local microstructure of the hard carbon samples, transmission electron microscopy (TEM) imaging of the hard carbon sample with pyrolysis temperature of 1300 °C was performed (**Figure 2**). Small nanodomains composed of curved graphitic layers with short-range stacking order can be observed. These characterizations indicate that the hydrothermal carbonization process yields typical hard carbon materials,^[19] whose structure may be tuned by high temperature annealing. The degree of order increases with higher pyrolysis temperature, while the increasing pore sizes likely originate from the fact that larger, more rigid graphitic areas

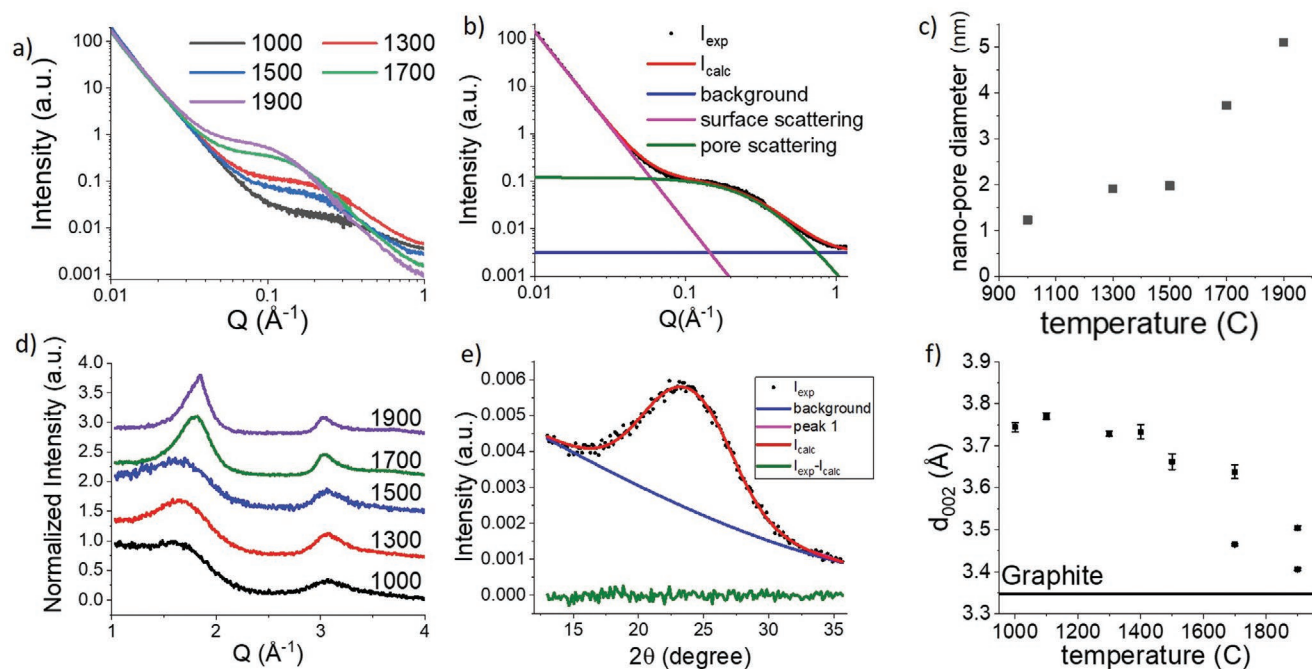


Figure 1. Structural characterization of hard carbon samples prepared at different pyrolysis temperatures. a) SAXS pattern for all samples showing a Guinier–Porod feature corresponding to nanopores of varying size and shape, b) example model fitting, and c) the extracted pore size.^[58] d) The WAXS pattern for all samples showing the characteristic two peaks of hard carbon corresponding to the 002 and 100 peaks of graphite. e) An example of a Gaussian peak fit to the 002 peak is included with the f) extracted interlayer distances.

are formed, resulting in larger void spaces in between these domains. From this analysis, the exact pore shapes are indeterminate, with both curved and planar pores contributing to the average pore size and shape.

The experimental characteristics of the as-synthesized hard carbon samples provide the foundation for the construction of computational models, which are discussed in detail in Sections 2.2–2.4 and the Experimental Section. To assess the effect of the different pore sizes and shapes on metal storage and diffusion, three different motifs were investigated computationally; planar graphitic stacks with interlayer distance 3.3–4 Å,

planar graphitic layer pores, and curved pores. The planar graphitic stacks and planar graphitic layer pores are modelled using the same basic model (Figure 9a), with different interlayer distance to capture both intercalation in the graphitic stacks, and metal behavior in planar graphitic pores with infinitely large graphitic layer separation. This separation will, range up to 8 Å, with a short discussion of separations up to 15 Å included.^[29,30] To assess the effect of curvature and pore size on metal storage, five different CNT models (representing cylindrical pores) with diameters ranging from 1 to 5 nm were constructed using the AtomsK code^[56] (177, 300, 420, 600, and 800 atoms for the 1, 2, 3, 4, and 5 nm diameter CNTs, respectively). The curvature of these CNT models represents curved pores in hard carbons with a radius of curvature of 0.5, 1, 1.5, 2, and 2.5 nm, respectively.

2.2. Metal Storage in the Planar Graphitic Layers

Figure 3 shows the calculated binding energy of Li, Na, and K in planar graphitic layers as a function of the interlayer distance. The calculations of the metal binding energy showed that all metals preferably adsorb on the HT site (as presented in Figure 9g in the computational details in the Experimental Section). The intercalation of Na and K in the planar graphitic layer with the tightest interlayer distance (3.35 Å) is energetically unfavorable, as indicated by positive binding energies of $E_{\text{int,Na}} = 0.82$ eV for Na and $E_{\text{int,K}} = 3.83$ eV for K. The binding energy of Li in this model of the 3.35 Å interlayer distance, is, however, negative, with $E_{\text{int,Li}} = -1.51$ eV, confirming the favorable intercalation of Li in this model.

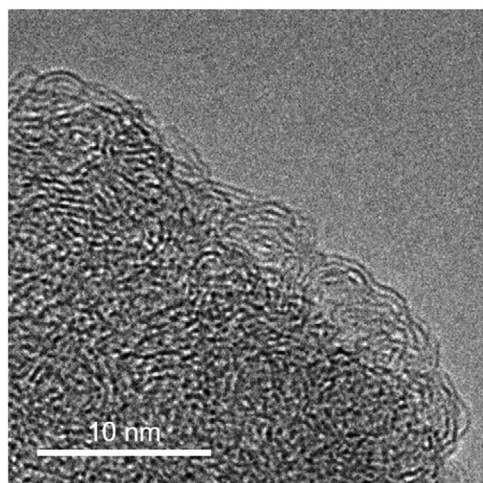


Figure 2. TEM image of the hard carbon sample with pyrolysis temperature of 1300 °C.

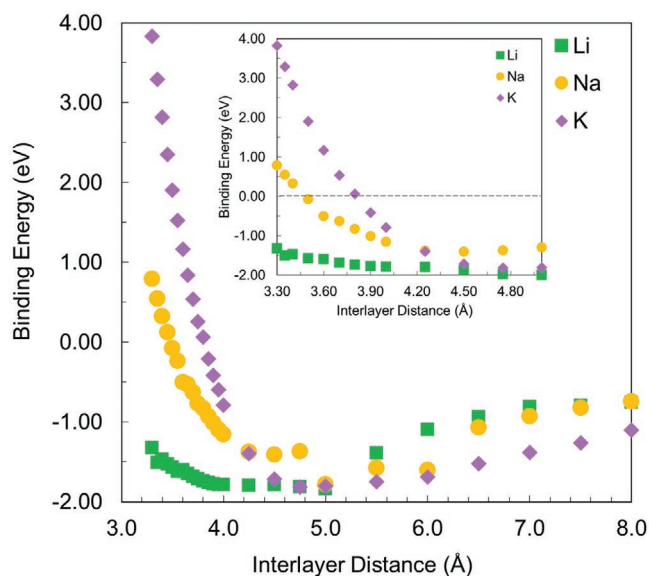


Figure 3. Li, Na, and K binding energy in the planar graphitic layers as a function of interlayer distance, with insert focusing on the shorter interlayer distances 3.30–5.0 Å to show the transition to energetically favorable (negative binding energy) Na and K intercalation.

From Figure 3, we can see that Li has negative binding energies in the planar graphitic layers for all the interlayer distances investigated, indicating that the insertion of Li in the planar graphitic layers is favorable. The intercalation energy of Na and K into the planar graphitic layers is directly dependent upon the interlayer distance, showing unfavorable intercalation at small interlayer distances ($c < 3.49$ Å for Na, and $c < 3.85$ Å for K), but favorable intercalation with expanding interlayer distance. Na incorporation into the two graphitic layers is energetically favorable (when $E_{\text{int,Na}} < 0$ eV) at $c = 3.49$ Å and above, while K intercalation energies become negative at an interlayer distance of 3.85 Å. Interestingly, the intercalation energies of Na and K are revealed to be similar at $c = 4.25$ Å ($E_{\text{int,Na}} = -1.38$ eV, and $E_{\text{int,K}} = -1.40$ eV), where after the K intercalation becomes more energetically favorable than Na intercalation. These conclusions are also observed experimentally, where in the high temperature materials G1700 and G1900, which have interlayer distances close to graphite, the lithium and sodium cells exhibit higher capacities than potassium (Figure S7, Supporting Information), due to the more favorable binding energies. In the lower temperature materials, where the interlayer distances are larger, Li insertion is still most favorable, but the difference is less pronounced between Na and K. Calculations of metal binding energies in planar graphitic layers with larger interlayer spacing (10 and 15 Å) were also conducted. The metal binding energies in the model with an interlayer space of $c = 10$ Å are -1.26 , -0.68 , and -1.11 eV for Li, Na, and K, respectively. The metal binding energies for the model with $c = 15$ Å were the same as on a single graphene layer (-1.22 , -0.62 , and -1.05 eV for Li, Na, and K, respectively^[35]). This indicates that when the interlayer distance is large enough, the adsorption strength of the metal in the two graphitic layers becomes similar to that on the graphene surface.

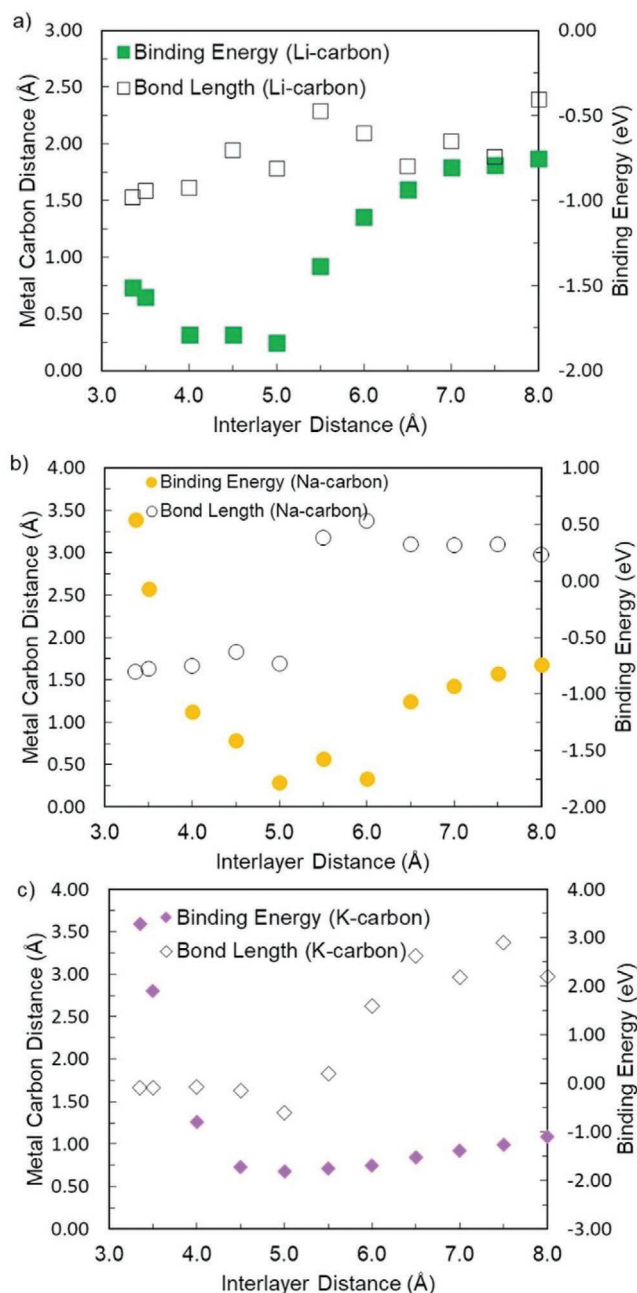


Figure 4. Metal carbon distance (left y-axis) and metal binding energy (right y-axis) as a function of interlayer spacing in the planar graphitic models for a) Li, b) Na, and c) K.

Studies on metal adsorption on graphene have shown that metal adsorption strength is correlated to the carbon-metal distance ($d_{\text{C-M}}$) and the metal ionization energy.^[35,37] From Figure 3, it is suggested that the metal binding energy strength decreases at $c > 5$ Å, to then approach the binding energies of metal on the graphene surface (when $c \geq 10$ Å). **Figure 4** shows $d_{\text{C-M}}$ as a function of interlayer distance, with the metal binding energies included on the secondary axes. From Figure 4 it is clear that Li (Figure 4a) shows the smallest range in $d_{\text{C-Li}}$ with interlayer distance (difference between minimum $d_{\text{C-Li}}$ and

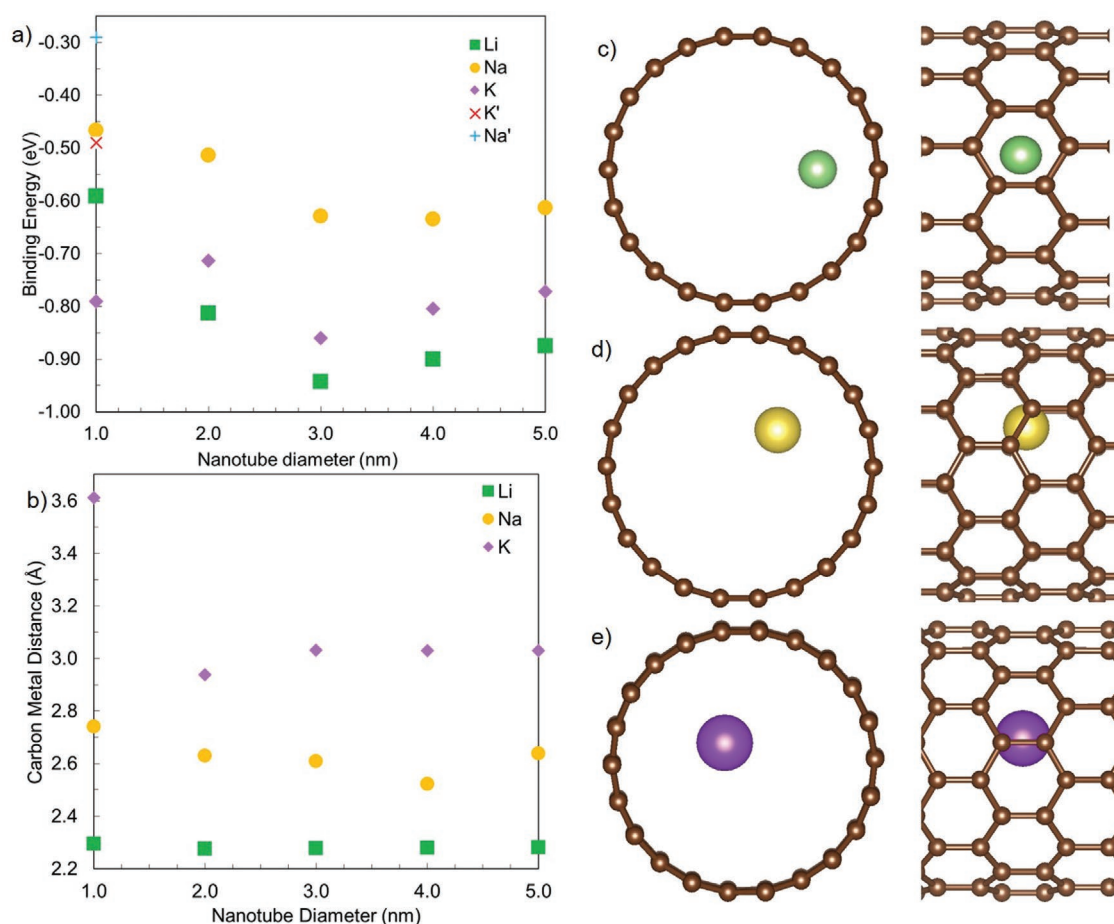


Figure 5. a) Binding energy of single metal ion in CNTs and b) carbon-metal distance as a function of nanotube diameter. For Na and K in the 1 nm CNT model, the lowest energy configuration is at the distorted B site, whereas for Na and K in all other CNT models here, the binding energy in (a) refers to Na and K on the H site. The binding energies of Na and K on the H site in the 1 nm CNT are indicated by Na' (blue +) and K' (red cross). These lowest energy structures of c) Li, d) Na, and e) K in 1 nm CNT are graphically represented. The left columns in (c–e) are top view (or through view) whereas the right columns in (c–e) are side views of the CNT. Brown spheres are carbon, green Li, yellow sodium, and purple is K. For all other CNT models, Na and K occupy the H site, as Li does in (c).

maximum $d_{\text{C-Li}}$ is 0.86 Å). The range in $d_{\text{C-Na}}$ (1.78 Å), and $d_{\text{C-K}}$ (2.00 Å) are much larger, showing a larger bond length dependence with interlayer spacing. Na (Figure 4b) and K (Figure 4c) both show two distinct $d_{\text{C-A}}$ regions, with the increase in $d_{\text{C-Na}}$ and $d_{\text{C-K}}$ observed at interlayer distances above 5 Å. Hence, the previously noted decrease in metal binding energy at $c > 5$ Å could be attributed to the larger metal carbon distance.

2.3. Metal Intercalation in Cylindrical Pores

To study the interaction of Li, Na, and K with cylindrical pores, single metal atoms were added to the inside of the CNTs (concave curvature). Simulations with the metals added to the outside of the nanotube (convex curvature) were also conducted. Since no meaningful difference was observed between the convex and concave curvatures for the larger CNT (4 and 5 nm), and the metal binding energies were stronger for the concave curvature, only the metal behavior inside the nanotube will be discussed here. Data for the convex curvature is

included in the supporting information (Table S1, Supporting Information). The calculated binding energies of Li, Na, and K in the CNT models are presented in Figure 5a, and in Table S2 in the Supporting Information. Li shows the strongest binding to the carbon lattice, with the binding strength following the trend $\text{Li} < \text{K} < \text{Na}$, mirroring that of Li, Na, and K adsorption on graphene.^[35] This trend was not seen in the planar graphitic layers, where the ionic radius of the metals was observed to have a larger influence on the binding energy than the difference between the ionization potentials of the metals (5.39 eV for Li, 5.14 eV for Na, and 4.32 eV for K).^[57] This would suggest that the Li, Na, and K storage mechanism in curved pores are more similar to the metal storage on graphene sheets. Comparing the adsorption energies of Li, Na, and K on graphene to the Li, Na, and K binding energies in the CNTs, none of the CNTs show as strong Li and K interactions. Hence, the curved graphenic sheets in hard carbon anodes do not have as high Li and K storage capacity as the flat graphene morphologies. Na in CNT shows binding energies close to the adsorption energy of Na on graphene (−0.62 eV), which could indicate that

Na storage is not decreased in curved hard carbon morphologies. This weaker Na binding may result in a greater metallic nature of these clusters stored within pores, as reflected in the more pronounced plateau close to 0 V observed in the Na voltage profile compared to Li and K, which is attributed to pore filling (Figure S7, Supporting Information).^[26,58] For the 1 nm CNT (Figure 5c–e), Li adsorbs above a C₆-unit (i.e., the hole site as shown in Figure 9h), whereas both Na and K bind most strongly above a carbon–carbon bond (i.e., the bridge site as shown in Figure 9h), with weaker binding energies for the adsorption of Na and K to the hole site. This could be attributed to the effect of different sizes of the metals, which makes Li readily accommodated in the C₆ ring, whereas the larger size of Na and K affects the favorable binding site at these small CNTs. Comparing the carbon–metal distances (Figure 5b), it is further seen that in the 1 nm CNT, the K–carbon lattice distance is much larger than at the CNTs of larger diameter. For CNTs with diameter >1 nm, the metal–carbon lattice distance remains constant, indicating that the smaller degree of curvature for the larger CNT diameters do not markedly influence the metal–carbon interaction.

2.4. Metal Migration

To investigate metal diffusion behavior in the planar graphitic layers and the CNT models, nudged elastic band (NEB) calculations have been employed to calculate the metal migration energy barriers using the method outlined in the Experimental Section. Experimental studies have shown that Na diffusion rates change with interlayer distance and with pore diameter in hard carbon anodes.^[29,30] A recent muon spin rotation spectroscopy study measured the average Na diffusion activation energy as 0.08 eV for a fully sodiated hard carbon.^[59] To evaluate the metal diffusion in different carbon motifs found in hard carbon, and to investigate if similar behavior would be expected for the Li and K diffusion in hard carbon, NEB calculations are used to calculate the metal migration barriers between two adjacent sites (resulting in two adjacent sites with the same binding energies presented in Figures 3 and 5) in the two models. **Figure 6** shows the migration barriers as a function of interlayer distance for the planar graphitic layer model, while **Figure 7** shows the migration barriers as a function of pore diameter for the CNT model. Hard carbon anodes do also show graphene basal plane diffusion, for which metal migration barriers have been published in a previous study.^[35] As a reference to the calculated migration barriers in the planar graphitic layers and in the CNT, the migration barrier on pristine graphene (or the basal plane) is 0.29 eV for Li, 0.10 eV for Na, and 0.09 eV for K.^[35]

2.4.1. Metal Migration in Planar Graphitic Layers

The metal migration barriers in the planar graphitic layers with different interlayer distances are presented in Figure 6. From Figure 6 it is clear that all metal migration barriers at all interlayer distances are below 0.5 eV. It is widely accepted that ≈0.5 eV is the threshold for atomic migration at room

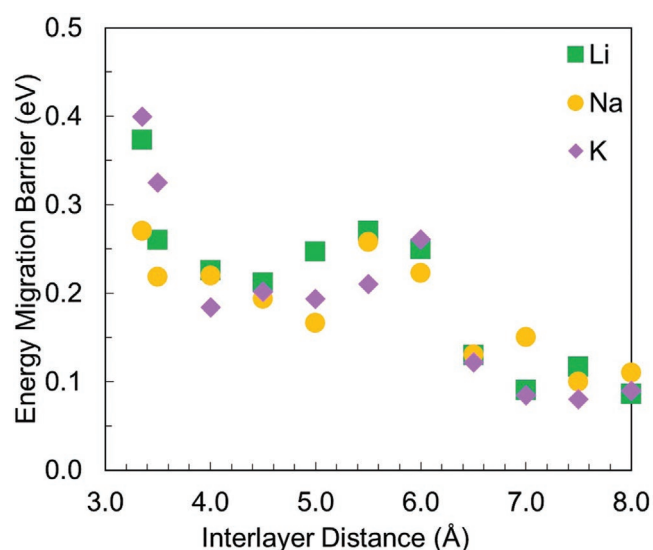


Figure 6. Metal energy migration barriers as a function of graphite interlayer distance in the planar graphitic layers model.

temperature, and hence all these migration barriers show that Li, Na, and K diffuse readily.^[60] Nevertheless, the actual magnitude of the metal migration barriers and their change with interlayer distance are important for the average diffusion rate.

The highest migration barriers in Figure 6 are seen for the planar graphitic models with interlayer distance 3.35–3.5 Å. As discussed above, Na and K intercalation becomes energetically favorable first at 3.49 and 3.85 Å, respectively. Hence, the much higher migration barriers at interlayer distances smaller than this would not contribute to experimentally measured average diffusion rates and would not hinder the diffusion of Na and K in hard carbon anodes. For the planar graphitic stacks (*c* between 3.3 and 4 Å), the mobility in terms of migration barrier is markedly increased at the larger interlayer distance. At these larger interlayer distances, a reduction of the Li migration barrier to 0.14 eV is observed, with both Na

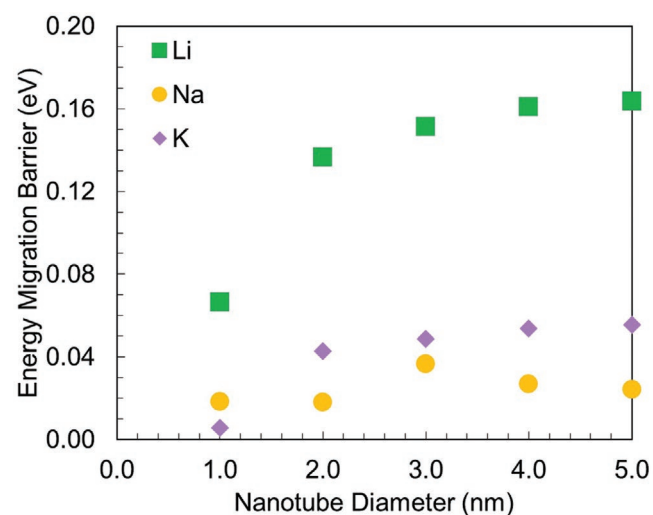


Figure 7. Metal energy migration barriers as a function of CNT diameter.

and K for the interlayer distances with favorable intercalation having migration barriers around 0.2 eV. The difference in metal migration at 4 Å where all three metals have energetically stable binding energies is small (migration barrier for Li is 0.23 eV, Na 0.22 eV, and K 0.18 eV). For the intermediate separation regime (4–6 Å), the metal migration barriers remain within a tight range of 0.06 eV for Li, 0.07 eV for Na and K. A sharp reduction of metal migration energies by >0.1 eV is then observed at an interlayer distance >6.5 Å. In these pores, metal diffusion is very rapid, and hence would contribute more to the overall diffusion of these metals in hard carbon anodes than the smaller interlayer distances. Considering the series of hard carbons annealed at different temperatures, it might therefore be expected that faster diffusion occurs in the low temperature annealed materials, and this effect can be observed when comparing their performance at different current densities when tested in a half-cell configuration (Figure S8, Supporting Information). For all the metals, the lowest temperature material, G1000, retains the highest capacity when cycled at a high current density (2C), because rapid diffusion can take place within the wide interlayer spacings. Conversely, in the material annealed at 1900 °C, the capacity is far lower, due to the limited diffusion in the narrower interlayer channels; these results are confirmed by electrochemical impedance spectroscopy (EIS), which indicates a higher cell resistance in the G1900 material than G1000 (Figure S9, Supporting Information). Comparing between the metals, Li has the lowest impedance and K the highest, which is consistent with the overall higher capacities achieved at 2C in the Li cells (Figure S8, Supporting Information). Given that the migration energies for all the metals within a graphite interlayer are similar, but the initial intercalation energy barrier for Na and K are higher than for Li, it is expected that the bottleneck for ion insertion in the cell arises from initial intercalation of metal ions between planar stacks, rather than from slow diffusion within the layers.

2.4.2. Metal Migration in Cylindrical Pores

Figure 7 shows the calculated metal migration energy barriers in the CNTs. The Li migration barriers increase with increasing CNT diameter, and are significantly higher than the Na and K migration energies. This behavior is in line with the stronger binding energies calculated for Li and the smaller Li-carbon distances. However, putting these Li migration barriers into context with the other hard carbon motifs, it is clear that Li migration in cylindrical pores and in curved pores contribute more to the overall Li diffusion rate than Li in graphitic stacks and graphenic basal planes. Na has the lowest energy barrier for migration, with its highest energy barrier (0.04 eV) being observed for CNTs with a diameter of 3 nm. The magnitude of these migration barriers suggests very rapid diffusion for Na in curved pores, and would be one of the main contributors to the average Na diffusion activation energies seen in hard carbon samples. K migration in the CNT with a diameter of 1 nm is very small, which is in line with the large K-carbon separation observed in Figure 5. As for Li, the K migration barriers are increasing with CNT diameter, but up to a maximum of 0.06 eV in the 5 nm CNT. Hence, from a device perspective,

curved pores would also be highly beneficial for metal transport through hard carbon anodes in KIBs.

Comparing the migration barriers of all metals in CNTs to those in the planar graphitic layers (as shown in Figure 7), it is clear that metal migration in the curved morphology would be expected to be faster than in the planar graphitic sheets. Hence, it is expected that metal diffusion coefficients in hard carbon anodes will have a larger contribution from metal migration on the curved morphologies, pores, and basal planes than from the graphitic stacks.

2.5. Metals in Mixed Planar and Curved Pores

Having studied the metal storage and migration of both planar and curved pores, it is clear that both morphologies would affect the anode performance. Planar graphitic pores contribute more to the metal storage than the curved pore morphologies, whereas the curved morphologies provide more rapid metal diffusion. As discussed in Section 2.1, the ratio of planar and curved pores in hard carbon, and how these are connected, remains unknown from the experimental characterization. To elucidate the metal binding at carbon motifs where the planar pores become curved (or vice versa), a simplified model is constructed to approximate the connected curved and planar regions (Figure 9c; Figure S10, Supporting Information). To construct these mixed morphology models, the aim was to include regions with narrow planar graphitic like pores (where curvature is very small), culminating in a region with curvature that can be approximated as a CNT. To achieve models with different degrees of curvature, and different planar to curved region ratios, a periodic folded graphene sheet (containing 800 atoms) model was constructed. This model is based on the reconstructed graphite surfaces described by Thinius et al.^[61] and Lechner et al.^[62] and is illustrated in Figure 9c in the computational details in the Experimental Section. To achieve models with different degree of curvature and planar-like graphitic regions, bilayer models (containing four graphene sheets) were relaxed to allow for surface reconstruction. Upon relaxation, the carbon edges reconstruct to form new interlayer bonds, maintaining the C₆-ring structure throughout the carbon model.^[62] A schematic to describe this is included in Figure S11 in the Supporting Information. To achieve different degrees of curvature, the cell width of the system (in the z-direction) was expanded. The first model has cell width 20 Å (corresponding to an initial interlayer distance between the graphene sheets of 5 Å), the second model has cell width 23 Å (corresponding to an initial interlayer distance of 5.75 Å), the third model cell width 25 Å (corresponding to an initial interlayer distance of 6.25 Å), and the fourth model cell width 27 Å (corresponding to an initial interlayer distance of 6.57 Å). A schematic of the relaxed structures of all these four models are included in Figure S12 in the Supporting Information, together with noted interlayer distances. For ease of reading, the four models will henceforth be referred to in terms of their cell width. Li, Na, and K binding at different regions were then probed on six different sites (Figure 9i), with the first metal binding position (P1) at the most planar region (most planar graphitic pore-like), and the sixth position (P6) being fully curved (CNT like). The

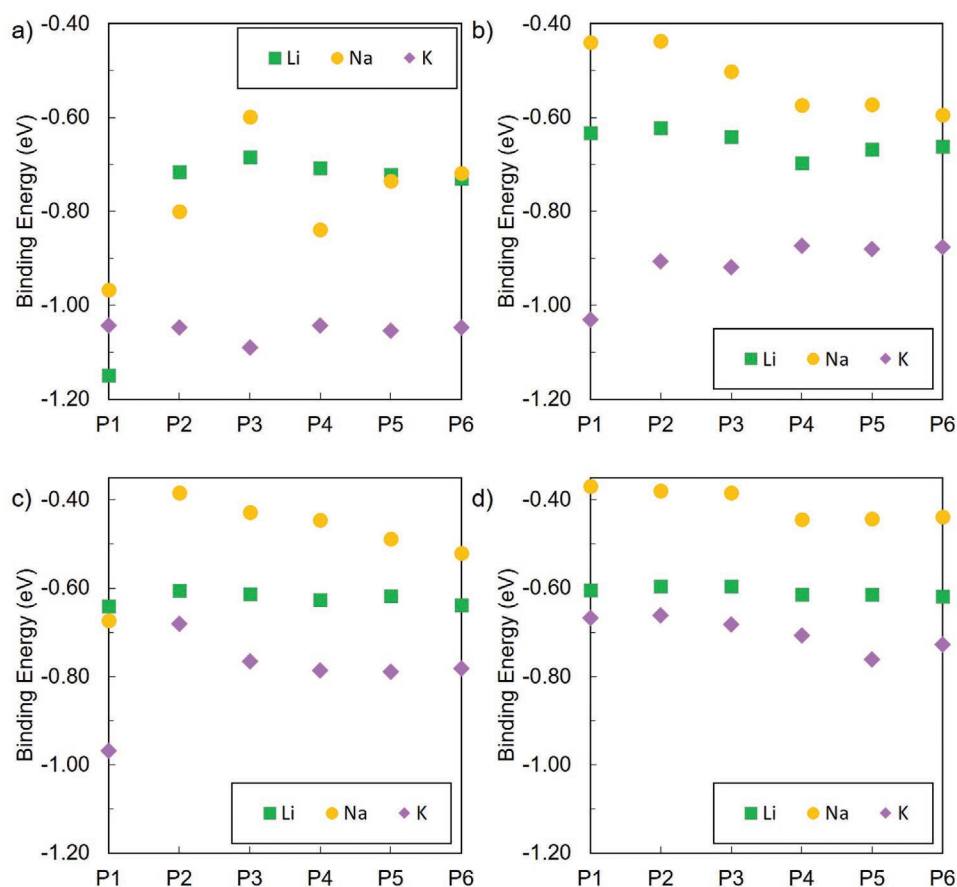


Figure 8. Metal binding energy as a function of different metal binding sites (P1, P2, P3, P4, P5, and P6 in Figure 9i) in the differently curved graphene sheet models with lattice parameter a) 20 Å, b) 23 Å, c) 25 Å, and d) 27 Å. P1 is the site with the least curvature (most planar graphitic layer model like) whereas P6 is the site with the most curvature (most cylindrical pore model like).

20 Å model has the most distinct division between planar (P1 and P2), transition region sites (P3 and P4), and maximum curvature at P5 and P6.

The calculated Li, Na, and K binding energies at different sites in the mixed planar and curved models are presented in **Figure 8** (the corresponding metal–carbon distances are included in Figure S13 in the Supporting Information). For the 20 Å model, the K binding energy remains graphene like (binding energy close to -1.05 eV) at all metal positions, whereas the Li binding energy becomes CNT like at the curved and transition regimes. Similar observations are made for Na in the 20 Å model. For the 23 Å, and 25 Å models K shows the strongest binding energy (similar to the expanded planar graphitic pores (Figure 3)), whereas Na is the most weakly bonded metal among the three. Li and Na show binding energies similar to those observed for the CNT models (Figure 5) for the 23 Å, and 25 Å models. Inspecting the metal carbon distances (Figure S13, Supporting Information), the Li carbon separation remains within a tight range, whereas the Na distance is more varied, and the transition moving from the planar to the curved morphologies can be clearly seen. Hence, the effect of having both curved and planar pores in the hard carbon anodes would have a larger impact on NIBs than LIBs. A similar observation can be made regarding the

K carbon distance for the 20 and 23 Å models, whereas the more expanded models (25 and 27 Å) do not induce this sharp shift in the K carbon distance. All metals show binding energies similar to those observed for the CNT models in the 27 Å model, indicating that the metal mobility in regions with these motifs would more closely resemble the behavior seen in CNTs (Section 2.4.2).

On the basis of this approximated model of a combined planar and curved carbon morphology model, which includes transition regions between the planar and curved pores, the metal behavior moving from the planar graphitic pores to the curved pores resembles, energetically, the behavior seen for the large expanded graphitic pores and the curved pores. Hence, metal mobility, based on the metal carbon distances and metal binding energies, would be expected to also be rapid in these regions, and to contribute towards the pore filling observed generally for hard carbon anodes. These combine to reduce the migration barriers as the degree of curvature increases the degree of curvature and the magnitude of the decrease in adsorption and migration energy is metal dependent. Hence, on the basis of energetics, the transition from purely planar to curved morphologies is more noticeable for the Na and K mobility and storage, than for Li which remains at a constant distance from the carbon surface.

3. Conclusion

In this paper, a study of Li, Na, and K storage and migration in different hard carbon morphologies was conducted to evaluate the effect of local structure on the metal behavior in hard carbon. Based on our experimentally synthesized hard carbon samples, different local carbon environments were identified for metal storage in the hard carbon anode materials. Atomic-scale models of the graphitic regions were constructed in terms of planar graphitic layers with interlayer distances ranging from 3.35 to 8.0 Å. To model curved morphologies, cylindrical pore models based on single-wall carbon nanotubes with different diameters were constructed. The effect of curvature, different carbon layer spacing, and pore diameters were clearly seen in the metal binding energies, with Li binding most strongly with the carbon lattice in all models, and Na and K requiring expanded interlayer spacing for energetically favorable bond formation in the planar graphitic layer models. This behavior is in agreement with experimental studies where Na and K storage capacity is higher in expanded graphitic layers than in pristine graphite. It also showed that these carbon motifs are promising as the base for anode materials in LIBs, NIBs, and KIBs, which will be further investigated in a future study.

The effect of curvature on metal storage was clearly seen in studying the metal adsorption in cylindrical pores, with Na and K preferably deviating from the commonly favorable H site at small pore diameters, and instead sitting above a B site. At cylindrical pore diameters ≥ 2 nm, Na and K binding on an H site returned to being the most energetically stable configuration. Comparing the metal binding energies on CNT to the planar graphitic layers model, it is clear that the metal storage in planar graphitic layers with intermediate and large interlayer distance is more favorable than metal storage in cylindrical pores. These weaker metal binding energies might, however, indicate that curved morphologies are more favorable for battery applications, as the more shallow energy wells would give better cycling capacity.

In addition to the metal storage capacity, the effect of carbon environment on the metal diffusion was studied in terms of metal migration barriers, and these results were experimentally observed when cycling the materials at high current densities. These calculations showed that the Li, Na, and K diffusion coefficients in hard carbon anodes have major contributions from curved morphologies and wide planar graphitic pores (interlayer distances above 6.5 Å). The contribution from the smaller graphitic stacks would be limited due to their high metal migration barriers.

In conclusion, a density functional theory (DFT) study evaluating the effect of different carbon environments in hard carbons on metal storage and diffusion has been carried out based on small-angle X-ray scattering/wide-angle X-ray scattering (SAXS/WAXS) and TEM structural characterization of hard carbon materials from glucose. It has been shown that on the basis of binding energy planar graphitic regions play an important role in the metal storage, whereas the curved pores aid rapid metal diffusion, with the shallow energy wells identified from the CNT weak Li, Na, and K binding energies contributing to good battery cycling performance, providing insight into how the various morphological features present in hard

carbons play important but disparate roles in the functioning of the anode.

4. Experimental Section

Experimental Methods: Hard carbon samples were synthesized by hydrothermal carbonization (HTC) of glucose (D-(+)-glucose, $\geq 99.5\%$, Sigma-Aldrich) (10 wt%) in deionized water. This solution was placed in a sealed autoclave reactor vessel (50% fill volume) and heated to 230 °C for 12 h, for carbonization. The resulting powder was dried under vacuum at 80 °C, and then further carbonized at varying temperatures between 1000 and 1900 °C for 2 h under a nitrogen atmosphere, to allow the effect of the pyrolysis temperature on the local structure to be explored.^[21] To characterize the hard carbon materials, powder X-ray diffraction (PXRD) measurements were performed on a Xenoc nano-Xrider using a Cu- k_{α} source, and a two-detector setup for simultaneous SAXS/WAXS measurement. The microstructure of the material carbonized at 1300 °C was observed by TEM, performed on a JEOL 2100Plus. The N_2 adsorption isotherms were obtained at 77 K using a Quantachrome NOVA 4200 instrument. The specific surface areas were calculated with the multipoint Brunauer–Emmett–Teller (BET) method, and pore volumes were obtained using a nonlocal density functional theory (NLDTF) model from the adsorption line of the isotherm.

All coin cell parts, 99.99% ethylene carbonate (EC), 99.99% dimethyl carbonate (DMC), 99.9% lithium hexafluorophosphate ($LiPF_6$), 99.5% sodium hexafluorophosphate ($NaPF_6$), and 99.9% potassium hexafluorophosphate (KPF_6), were purchased from Guangdong Canrd New Energy Technology Co., Ltd. Lithium metal (granular, 99% trace metals basis), sodium carboxymethyl cellulose binder ($M_w \approx 250\,000$), potassium chunks (98% trace metals basis) and Whatman GF/D glass microfiber were purchased from Sigma Aldrich. Sodium ingot (99.8% metals basis) were purchased from Alfa Aesar. All chemicals were used as received without any further treatment.

All electrodes were prepared from slurries (90 wt% hard carbon, 10 wt% sodium carboxymethyl cellulose binder ($M_w \approx 250\,000$) in water) applied on a Cu foil (9 μm , MTI corporation). The loading mass of an electrode was ≈ 2 mg cm^{-2} . The electrodes were tested in a coin cell configuration against lithium metal, sodium metal or potassium metal, and separated by a Whatman GF/D glass microfiber separator saturated with a 1 M electrolyte solution of $LiPF_6$, $NaPF_6$ and KPF_6 , respectively, in a 1:1 mixture, by volume, of ethylene carbonate and dimethyl carbonate.

Computational Methods: Two different hard carbon morphologies were investigated: parallel planar graphitic layers, and cylindrical pores, which were represented by single-wall carbon nanotubes. To model metal storage and migration in the planar graphitic layers, a $4 \times 4 \times 2$ supercell (64 atoms) was used, with one metal atom added in between the two planar graphitic layers to study intercalation and migration. The two planar graphitic layers were placed in an AB stacking mode, while varying the interlayer distance c (c lattice parameter) to investigate the effect of different interlayer distances on metal migration and binding. A graphical representation of the planar graphitic layer model is included in Figure 9a,d.

Apart from the planar graphitic layers, there were micro- and mesopores in nanometer scale and rimped/curved structures in hard carbon anodes. Curved pores have been observed experimentally from pair distribution function analysis and TEM imaging, and is thought to have a large effect on the Na storage capabilities in hard carbon NIB anodes.^[26] It has also been reported that curved graphitic sheets in hard carbon have an average radius of curvature of 1.6 nm.^[41] To model metal ion behavior in these curved graphitic environments, CNT models were constructed using the AtomsK code^[56] to represent cylindrical pores with curvature. The CNT models were all based upon the zigzag terminated buckytube structures, and each structure had a long dimension of 1.6 nm, and the long axis of the tube ran in the z -direction and was periodic (Figure 9b). There was a minimum separation between periodic images of 20 Å (converged vacuum gap 15 Å) in the x - and y -directions.

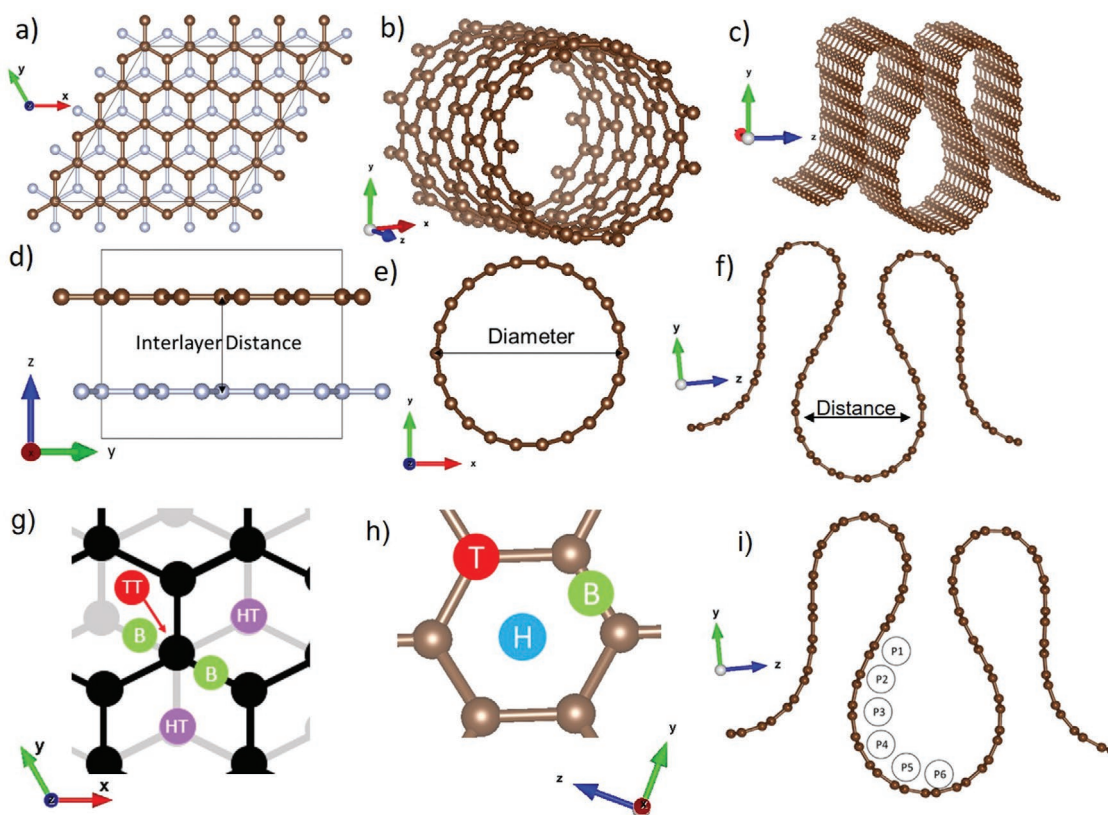


Figure 9. Schematic representations of the a) planar graphitic layer model and b) cylindrical pore (single-walled carbon nanotube) model, and c) mixed planar and curved models, with d–f) the interlayer distances and diameter, respectively, for each model. Figures were made using the VESTA software.^[86] Schematic illustration of the inequivalent metal adsorption sites on g) planar graphitic layer and h) in the cylindrical pore model. i) The metal binding site positions on the mixed planar and curved models as referenced in Figure 8. Brown and grey spheres are carbon (in alternating layers in the planar graphitic model), the grey lines and dots in (e) represent one planar graphitic layer, and the black the second planar graphitic layer. The green, red, blue, and purple dots in (e) and (f) represent inequivalent metal binding sites in the models. The blue dot represents metal site above the center of a hexagonal C₆-ring (hole site denoted H), the red dot represents metal site above a carbon atom (top site denoted T in (f), and TT in (e)), and the green dots show metal site above (or below depending on reference layer in a) a C–C bond (bridge site denoted B). The purple dots are a combination of the T and H site (denoted HT), where the metal site in one of the planar graphitic layers sits above a hole site, and in the second planar graphitic layer sits below a top site (or vice versa).

The binding or intercalation of a metal (denoted A) in the carbon models was evaluated by calculating the metal binding energy, E_b (Equation 1)

$$E_b = E_{A \text{ on carbon}} - \mu_A - E_{\text{carbon}} \quad (1)$$

$E_{A \text{ on carbon}}$ is the total energy of the carbon models with added metal A, E_{carbon} is the total energy of the carbon system without metal ion, and μ_A is the chemical potential of A, calculated as the total energy of one A isolated in a $20 \text{ \AA} \times 20 \text{ \AA} \times 20 \text{ \AA}$ vacuum box. Following this convention, a negative binding energy showed that the bonding of A to the carbon structure was energetically favorable, whereas a positive value indicated an unfavorable bonding process. To investigate the metal ion intercalation behavior in the planar graphitic layers with varying interlayer distance and in cylindrical pores with different diameters, the metal binding energy was calculated on different inequivalent lattice sites (Figure 9g,h): bridge (denoted B), hole (denoted H), and top (denoted T). For the cylindrical pore mode, these three different adsorption sites were clearly labeled in Figure 9h. For the planar graphitic layer model, there were several complex cases with the adsorption sites, due to the offset of the two graphitic layers. The B sites were always layer-independent, meaning that when a metal was inserted in between the two graphitic layers, it could either be adsorbed to a B site of the top layer or a B site of the bottom layer, with the two B sites having different coordinate positions on the x–y plane. There were also combinations of different

sites. For example, a metal could be adsorbed to a hole site of the top layer while at the same time being adsorbed to a top site of the bottom layer, with the two sites having the same coordinates on the x–y plane but being kept apart by the layer distance. Such sites were denoted as HT sites. In other cases, the metal can be adsorbed to a T site of the top layer, while at the same time being adsorbed to a top site of the bottom layer, with the two T sites having the same coordinates on the x–y plane but being kept apart by the layer distance. Such sites were denoted as TT sites. Apart from the B sites, HT, and TT sites, there were also independent H sites and T sites, on the top layer and the bottom layer respectively. Metal adsorption on all these different sites was considered in the DFT simulations. Hence, the metal intercalation and migration in the planar graphitic layers will present a different chemical environment to that on the CNTs.

For the atomic scale simulations of Li, Na, and K incorporation and diffusion in the planar graphitic layers, calculations were made using DFT in the Vienna Ab initio Simulation Package (VASP, version 5.3.5).^[63–66] These periodic DFT calculations utilized the projector-augmented wave method (PAW) to model the ion-electron interaction.^[67] The plane wave cutoff and k-space integrals were chosen so that the total energy was converged to 1 meV per atom. The kinetic energy cutoff was then after convergence tests put to 800 eV, with a $5 \times 5 \times 2$ Γ -centered Monkhorst–Pack grid to sample the Brillouin zone.^[68] The exchange-correlation energy (with electronic convergence criteria of 10^{-5} eV and ionic

convergence criteria of 10^{-3} eVÅ⁻¹) was described by the generalized gradient approximation (GGA) with Perdew–Burke–Ernzerhof (PBE)^[69,70] functional. Furthermore, all calculations were spin-polarized.^[71] Due to the large polarizability of the graphitic planes and the metals,^[72] it was essential to include dispersion corrections to accurately estimate the metal adsorption strength, and interlayer binding energy.^[73–75] Weak van der Waals forces between the graphitic sheets have been accounted for by the DFT-D3 method with Becke–Johnson damping by Grimme and co-workers.^[76] This setup was previously used to study the adsorption and migration of Li, Na, and K on graphene, and its performance has been verified previously in the literature.^[72,77]

The calculations of the CNTs and the mixed planar and curved models were performed with the CP2K code (which enables the simulations of large systems),^[78–81] with the same PBE functional and the DFT-D3 method with Becke–Johnson damping for the dispersion correction, as with the calculations performed using VASP for the planar graphitic layers. The calculations were all performed at the Γ -point with a plane wave cutoff of 650 Ry and the TZVP-SR-MOLOPT^[79,82] basis set. All parameters were converged to 0.01 meV with respect to energy and 0.001 eV Å⁻¹ with respect to forces.

For both the planar graphitic layers and the CNT cylindrical pore models, metal migration energy barrier calculations were performed using the climbing image nudged elastic band method (CI-NEB), which was implemented in both VASP and CP2K. The metal migration paths were created using the VASP Transition State Tools.^[83] From the CI-NEB calculations, the metal migration energy barrier was taken as the maximum energy difference between the initial and final states on the migration paths.^[84,85]

Supporting Information

Supporting Information is available from the Wiley Online Library or from the author.

Acknowledgements

The authors would like to thank the Engineering and Physical Sciences Research Council for funding (Grant No. EP/R021554/1). E.O. would like to acknowledge the use of Athena at HPC Midlands+, which was funded by the EPSRC under grant EP/P020232/1, and the Eureka HPC cluster at the University of Surrey. The authors are grateful to the UK Materials and Molecular Modelling Hub for computational resources, which was partially funded by EPSRC (Grant No. EP/P020194/1). Z.G. would like to thank China Scholarship Council (CSC) for the scholarship. The authors would like to thank Dr. Gavin Stenning for help on the Nano InXider instrument in the Materials Characterization Laboratory at the ISIS Neutron and Muon Source.

Conflict of Interest

The authors declare no conflict of interest.

Author Contributions

E.O., J.C., H.Au., and Z.G. contributed equally to this work. E.O. designed the study and drafted the article. E.O. and J.C. conducted the DFT simulations and analysis. J.C., H.Au., H.Ai., and A.C.S.J. revised and edited the manuscript. H.Au. and H.Ai. developed and synthesized the hard carbon samples, and conducted the electrochemical testing for the NIB cells, the N₂ adsorption, and BET measurements. H.Au. obtained the TEM image. A.C.S.J. conducted the PXRD, SAXS, and WAXS measurements and analysis. Z.G. conducted the cyclic voltammetry

(CV), galvanostatic charge/discharge (GCD), rate performance, and EIS of hard carbon samples in Li-, Na-, and K-ion batteries. A.J.D., M.-M.T., and Q.C. provided supervision and funding, and revised and edited the final manuscript.

Keywords

batteries, density functional theory, metal diffusion, metal storage

Received: October 4, 2019

Revised: January 14, 2020

Published online: February 28, 2020

- [1] S. Takeuchi, T. Fukutsuka, K. Miyazaki, T. Abe, *Carbon* **2013**, 57, 232.
- [2] S. Komaba, T. Hasegawa, M. Dahbi, K. Kubota, *Electrochem. Commun.* **2015**, 60, 172.
- [3] Y. Li, Y. Lu, P. Adelhelm, M.-M. Titirici, Y.-S. Hu, *Chem. Soc. Rev.* **2019**, 48, 4655.
- [4] O. Lenchuk, P. Adelhelm, D. Mollenhauer, *Phys. Chem. Chem. Phys.* **2019**, 21, 19378.
- [5] W. Luo, J. Wan, B. Ozdemir, W. Bao, Y. Chen, J. Dai, H. Lin, Y. Xu, F. Gu, V. Barone, L. Hu, *Nano Lett.* **2015**, 15, 7671.
- [6] Z. Jian, Z. Xing, C. Bommier, Z. Li, X. Ji, *Adv. Energy Mater.* **2016**, 6, 1501874.
- [7] M. Chen, W. Wang, X. Liang, S. Gong, J. Liu, Q. Wang, S. Guo, H. Yang, *Adv. Energy Mater.* **2018**, 8, 1800171.
- [8] E. Buiel, J. R. Dahn, *Electrochim. Acta* **1999**, 45, 121.
- [9] V. G. Pol, J. Wen, K. C. Lau, S. Callear, D. T. Bowron, C. K. Lin, S. A. Deshmukh, S. Sankaranarayanan, L. A. Curtiss, W. I. F. David, D. J. Miller, M. M. Thackeray, *Carbon* **2014**, 68, 104.
- [10] N. A. Kaskhedikar, J. Maier, *Adv. Mater.* **2009**, 21, 2664.
- [11] J. C. Pramudita, D. Sehwat, D. Goonetilleke, N. Sharma, *Adv. Energy Mater.* **2017**, 7, 1602911.
- [12] Y. Li, R. A. Adams, A. Arora, V. G. Pol, A. M. Levine, R. J. Lee, K. Akato, A. K. Naskar, M. P. Paranthaman, *J. Electrochem. Soc.* **2017**, 164, A1234.
- [13] K. Omichi, G. Ramos-Sanchez, R. Rao, N. Pierce, G. Chen, P. B. Balbuena, A. R. Harutyunyan, *J. Electrochem. Soc.* **2015**, 162, A2106.
- [14] B. Hu, K. Wang, L. Wu, S. H. Yu, M. Antonietti, M.-M. Titirici, *Adv. Mater.* **2010**, 22, 813.
- [15] F. Wen, J. Xiang, J. Zhao, L. Wang, Z. Liu, W. Lv, Y. Tian, L. Li, *Electrochim. Acta* **2015**, 176, 533.
- [16] K. Wang, Y. Jin, S. Sun, Y. Huang, J. Peng, J. Luo, Q. Zhang, Y. Qiu, C. Fang, J. Han, *ACS Omega* **2017**, 2, 1687.
- [17] C. Bommier, X. Ji, *Isr. J. Chem.* **2015**, 55, 486.
- [18] M. Genovese, J. Jiang, K. Lian, N. Holm, *J. Mater. Chem. A* **2015**, 3, 2903.
- [19] Z. Li, Z. Jian, X. Wang, I. A. Rodríguez-Pérez, C. Bommier, X. Ji, *Chem. Commun.* **2017**, 53, 2610.
- [20] N. Zhang, Q. Liu, W. Chen, M. Wan, X. Li, L. Wang, L. Xue, W. Zhang, *J. Power Sources* **2018**, 378, 331.
- [21] K. Jurkiewicz, S. Duber, H. E. Fischer, A. Burian, *J. Appl. Crystallogr.* **2017**, 50, 36.
- [22] R. E. Franklin, *Acta Crystallogr.* **1951**, 4, 253.
- [23] B. Zhang, C. M. Ghimbeu, C. Laberty, C. Vix-Guterl, J. M. Tarascon, *Adv. Energy Mater.* **2016**, 6, 1501588.
- [24] D. A. Stevens, J. R. Dahn, *J. Electrochem. Soc.* **2000**, 147, 1271.
- [25] C. Matei Ghimbeu, J. Górká, V. Simone, L. Simonin, S. Martinet, C. Vix-Guterl, *Nano Energy* **2018**, 44, 327.
- [26] J. M. Stratford, P. K. Allan, O. Pecher, P. A. Chater, C. P. Grey, *Chem. Commun.* **2016**, 52, 12430.

- [27] P. Bai, Y. He, X. Zou, X. Zhao, P. Xiong, Y. Xu, *Adv. Energy Mater.* **2018**, 8, 1703217.
- [28] C. Bommier, W. Luo, W. Y. Gao, A. Greaney, S. Ma, X. Ji, *Carbon* **2014**, 76, 165.
- [29] M. Dahbi, M. Kiso, K. Kubota, T. Horiba, T. Chafik, K. Hida, T. Matsuyama, S. Komaba, *J. Mater. Chem. A* **2017**, 5, 9917.
- [30] S. Alvin, D. Yoon, C. Chandra, H. S. Cahyadi, J. H. Park, W. Chang, K. Y. Chung, J. Kim, *Carbon* **2019**, 145, 67.
- [31] H. Zheng, Q. Qu, L. Zhang, G. Liu, V. S. Battaglia, *RSC Adv.* **2012**, 2, 4904.
- [32] K. Chayambuka, G. Mulder, D. L. Danilov, P. H. L. Notten, *Adv. Energy Mater.* **2018**, 8, 1800079.
- [33] Z. Ju, P. Li, G. Ma, Z. Xing, Q. Zhuang, Y. Qian, *Energy Storage Mater.* **2018**, 11, 38.
- [34] Y. Zhai, Y. Dou, D. Zhao, P. F. Fulvio, R. T. Mayes, S. Dai, *Adv. Mater.* **2011**, 23, 4828.
- [35] E. Olsson, G. Chai, M. Dove, Q. Cai, *Nanoscale* **2019**, 11, 5274.
- [36] A. Karatrantos, Q. Cai, *Phys. Chem. Chem. Phys.* **2016**, 18, 30761.
- [37] A. Karatrantos, S. Khan, T. Ohba, Q. Cai, *Phys. Chem. Chem. Phys.* **2018**, 20, 6307.
- [38] Z. Jian, C. Bommier, L. Luo, Z. Li, W. Wang, C. Wang, P. A. Greaney, X. Ji, *Chem. Mater.* **2017**, 29, 2314.
- [39] Y. Zhang, L. Yang, Y. Tian, L. Li, J. Li, T. Qiu, G. Zou, H. Hou, X. Ji, *Mater. Chem. Phys.* **2019**, 229, 303.
- [40] F. Xie, Z. Xu, A. C. S. Jensen, H. Au, Y. Lu, V. Araullo-Peters, A. J. Drew, Y. S. Hu, M.-M. Titirici, *Adv. Funct. Mater.* **2019**, 29, 1901072.
- [41] X. Dou, I. Hasa, D. Saurel, C. Vaalma, L. Wu, D. Buchholz, D. Bresser, S. Komaba, S. Passerini, *Mater. Today* **2019**, 23, 87.
- [42] Z. Li, C. Bommier, Z. Sen Chong, Z. Jian, T. W. Surta, X. Wang, Z. Xing, J. C. Neuefeind, W. F. Stickle, M. Dolgos, P. A. Greaney, X. Ji, *Adv. Energy Mater.* **2017**, 7, 1602894.
- [43] X. Dou, I. Hasa, D. Saurel, M. Jauregui, D. Buchholz, T. Rojo, S. Passerini, *ChemSusChem* **2018**, 11, 3276.
- [44] X. Dou, I. Hasa, M. Hekmatfar, T. Diemant, R. J. Behm, D. Buchholz, S. Passerini, *ChemSusChem* **2017**, 10, 2668.
- [45] Q. Wei, F. Xiong, S. Tan, L. Huang, E. H. Lan, B. Dunn, L. Mai, *Adv. Mater.* **2017**, 29, 1602300.
- [46] S. Licht, A. Douglas, J. Ren, R. Carter, M. Lefler, C. L. Pint, *ACS Cent. Sci.* **2016**, 2, 162.
- [47] Y. Liang, W. H. Lai, Z. Miao, S. L. Chou, *Small* **2018**, 14, 1702514.
- [48] B. J. Landi, M. J. Ganter, C. D. Cress, R. A. DiLeo, R. P. Raffaele, *Energy Environ. Sci.* **2009**, 2, 638.
- [49] Y. Chen, X. Li, K. Park, J. Song, J. Hong, L. Zhou, Y. W. Mai, H. Huang, J. B. Goodenough, *J. Am. Chem. Soc.* **2013**, 135, 16280.
- [50] S. H. Ng, J. Wang, Z. P. Guo, J. Chen, G. X. Wang, H. K. Liu, *Electrochim. Acta* **2005**, 51, 23.
- [51] C. De Las Casas, W. Li, *J. Power Sources* **2012**, 208, 74.
- [52] M.-S. S. Balogun, Y. Luo, W. Qiu, P. Liu, Y. Tong, *Carbon* **2016**, 98, 162.
- [53] E. Steinbauer, A. Schinner, O. Benka, *Beam Interactions with Materials and Atoms*, Vol. 171, Elsevier, Amsterdam **2000**, p. 291.
- [54] M. S. Khan, A. V. Karatrantos, T. Ohba, Q. Cai, *Phys. Chem. Chem. Phys.* **2019**, 21, 22722.
- [55] S. Jiang, Y. Li, Y. Qian, J. Zhou, T. Li, N. Lin, Y. Qian, *J. Power Sources* **2019**, 436, 226847.
- [56] P. Hirel, *Comput. Phys. Commun.* **2015**, 197, 212.
- [57] K. Rytönen, J. Akola, M. Manninen, *Phys. Rev. B* **2007**, 75, 075401.
- [58] D. A. Stevens, J. R. Dahn, *J. Electrochem. Soc.* **2000**, 147, 4428.
- [59] A. C. S. Jensen, E. Olsson, H. Au, H. Alptekin, Z. Yang, S. Cottrell, K. Yokoyama, Q. Cai, M.-M. Titirici, A. J. Drew, *J. Mater. Chem. A* **2020**, 8, 743.
- [60] K. Nakada, A. Ishii, *Solid State Commun.* **2011**, 151, 13.
- [61] S. Thinius, M. M. Islam, T. Bredow, *Surf. Sci.* **2016**, 649, 60.
- [62] C. Lechner, P. Baranek, H. Vach, *Carbon* **2018**, 127, 437.
- [63] G. Kresse, J. Hafner, *Phys. Rev. B* **1993**, 47, 558.
- [64] G. Kresse, J. Hafner, *Phys. Rev. B* **1994**, 49, 14251.
- [65] G. Kresse, J. Furthmüller, *Comput. Mater. Sci.* **1996**, 6, 15.
- [66] G. Kresse, J. Furthmüller, *Phys. Rev. B* **1996**, 54, 11169.
- [67] P. E. Blöchl, *Phys. Rev. B* **1994**, 50, 17953.
- [68] H. J. Monkhorst, J. D. Pack, *Phys. Rev. B* **1976**, 13, 5188.
- [69] J. Perdew, K. Burke, M. Ernzerhof, *Phys. Rev. Lett.* **1996**, 77, 3865.
- [70] J. Perdew, K. Burke, M. Ernzerhof, *Phys. Rev. Lett.* **1997**, 78, 1396.
- [71] Y. Ma, P. O. Lehtinen, A. S. Foster, R. M. Nieminen, *New J. Phys.* **2004**, 6, 68.
- [72] X. Fan, W. T. Zheng, J. L. Kuo, *ACS Appl. Mater. Interfaces* **2012**, 4, 2432.
- [73] X. Fan, W. T. Zheng, J.-L. L. Kuo, D. J. Singh, *ACS Appl. Mater. Interfaces* **2013**, 5, 7793.
- [74] M. Amft, S. Lebègue, O. Eriksson, N. V. Skorodumova, *J. Phys.: Condens. Matter* **2011**, 23, 395001.
- [75] S. Lee, M. Lee, H. Choi, D. S. Yoo, Y. C. Chung, *Int. J. Hydrogen Energy* **2013**, 38, 4611.
- [76] S. Grimme, S. Ehrlich, L. Goerigk, *J. Comput. Chem.* **2011**, 32, 1456.
- [77] S. Thinius, M. M. Islam, P. Heitjans, T. Bredow, *J. Phys. Chem. C* **2014**, 118, 2273.
- [78] J. VandeVondele, M. Krack, F. Mohamed, M. Parrinello, T. Chassaing, J. Hutter, *Comput. Phys. Commun.* **2005**, 167, 103.
- [79] J. VandeVondele, J. Hutter, *J. Chem. Phys.* **2007**, 127, 114105.
- [80] J. Hutter, M. Iannuzzi, F. Schiffmann, J. VandeVondele, *Wiley Interdiscip. Rev.: Comput. Mol. Sci.* **2014**, 4, 15.
- [81] K. Burke, F. G. Cruz, K.-C. Lam, *J. Chem. Phys.* **1998**, 109, 8161.
- [82] M. Guidon, J. Hutter, J. VandeVondele, *J. Chem. Theory Comput.* **2010**, 6, 2348.
- [83] G. Henkelman, VTST Tools, <http://theory.cm.utexas.edu/vtsttools/> (accessed: August 2016).
- [84] G. Henkelman, B. P. Uberuaga, H. Jónsson, *J. Chem. Phys.* **2000**, 113, 9901.
- [85] G. Henkelman, H. Jónsson, *J. Chem. Phys.* **2000**, 113, 9978.
- [86] K. Momma, F. Izumi, *J. Appl. Crystallogr.* **2011**, 44, 1272.